Experimental assessment of scale-effects on the aerodynamic characterisation of a transitionally-operating airfoil working under clean flow conditions

Abstract

Wind tunnel tests are carried out upon a NACA0021 airfoil subjected to transitional Reynolds numbers. Transitionally-operating airfoils show a high sensitivity to external conditions and pose relevant measurement issues for capturing the physical processes adequately. On the global side, the employed set of techniques measures lift forces directly and uses the momentum-deficit method for drag coefficients. Locally, the development of transitional structures is acknowledged via surface pressure measurements carried out by pressure taps together with oil-flow visualizations. The coupling of such techniques with a well-founded uncertainty analysis shows two relevant aspects of the measurement protocolization: on the one hand, the limitations of either the global or local methods for completely accounting for all transitional phenomena. On the other hand, the fact that combining the proposed set of different measurement techniques with a systematic protocol is a mandatory requirement for achieving a holistic characterisation of transitionally-operating airfoils.

Keywords: wind tunnel testing, transitional regime, flow measurement techniques, uncertainty analysis

1. Introduction

Micro- and nano-aerial-vehicles (MAVs and UAVs, respectively), wind turbines or turbomachinery devices share two main features. The first has to do with their working principle, which relies on aerodynamics. The second is that MAV-UAV wings, turbine blades or turbomachinery vanes operate within the transitional flow regime [1–10]. Mentioning such a regime implies setting a constraint on the possible values adopted by the Reynolds number of the flow. This number is a ratio between the convective (velocity-driven) and viscous forces that act upon a device immersed in a fluid, i.e. $\mathrm{Re} = \rho U L/\mu$, where ρ and μ stand for the fluid's density and viscosity, respectively, while U and L are the characteristic velocity- and length-scales of the configuration. The order of magnitude of the Reynolds number provides information on the physical processes that govern the flow [11].

The aerodynamic capabilities of streamlined bodies such as wings, blades or vanes result from their particular cross-sectional shape. This shape, termed as an airfoil, is considered the main object of the aerodynamic analysis. The Reynolds number of the mentioned devices is calculated by setting the characteristic length (L) to the chord (c) of the airfoil, which corresponds to the streamwise dimension of the body when it is oriented parallel to the flow. In external flows, an airfoil may operate in three possible flow regimes depending on the value of the Reynolds number: for $\mathrm{Re} \lesssim 10^4$ the regime is laminar, with the flow streamlines developing in a layered manner. On the other end of the interval, for $\mathrm{Re} \approx 10^6 - 10^7$, the regime is turbulent, with the streamlines undergoing an appreciable mixing and forming a disordered set of eddies. Transitional flows stand in between, spanning the range $10^4 < \mathrm{Re} < 10^6$ [4, 12]. The first two regimes are relatively well understood currently, but the transitional one shows complex interplays between laminar and turbulent structures, as well as a strong dependence with respect to external flow conditions. Factors such as freestream turbulence [3, 13–15] or environmentally-induced roughness [16–19] are present in the scenarios at which transitionally-operating airfoils work, and they affect their behaviour severely. However, those factors turn the aerodynamic analysis complex, and it is common to limit the research to a simpler configuration, namely the clean-flow paradigm, within which turbulence and roughness effects are not considered. And even under such circumstances, transitionally-operating airfoils remain highly sensitive to the most fundamental of the flow parameters, namely the Reynolds number, whose variations induce relevant changes on the aerodynamic behaviour [5, 12, 20–25].

This scale-effect, as it is termed, is usually ascribed to the development of laminar separation bubbles (LSBs) upon the suction-side of the airfoil [12, 23–25]. These constitute regions of the surface that show a separated flow pattern, which nevertheless manages to reattach in the form of a re-energised turbulent boundary-layer further downstream [12]. The inherently unstable nature of LSBs, and their high sensitivity to external conditions, causes the airfoils to show the mentioned scale-effect. When designing transitionally-operating airfoils, such a sensitivity requires characterising their behaviour under a thorough set of possible operation conditions. For the clean flow paradigm, such conditions are established by variations in the Reynolds number itself (the mentioned scale-effect) and in the angle-of-attack (α) of the airfoil. A detailed characterisation determines the evolutions of the aerodynamic loads of the airfoil with the mentioned flow parameters, i.e. the lift (c_l) and drag coefficients (c_d), on the one hand. And the evolutions of surface pressure-coefficient distributions ($c_p(x)$) as well as the changes in flow patterns produced by them, on the other hand. In a concise mathematical form, the aim would be to obtain the expressions $(c_l, c_d, c_p(x)) = f(\alpha, \mathrm{Re})$. The evolutions of the load coefficients provide the global behaviour of the airfoil, as they show how much power can be obtained from the system. The c_p distributions and flow patterns constitute the local approach, and are relevant for addressing the mechanisms that drive the scale-effect.

There are two main problems with such a characterisation approach. The first is that measurements turn highly dependent on the conditions of the flow, as is the feature of the transitional regime. The consequence of such a dependence is that addressing the short-ranged scale-effect becomes complex. Differences between curves obtained at Reynolds numbers that differ a relatively large amount does not pose a problem, but reducing such an amount below a given threshold makes the curves experimentally undiscernible, unless a proper uncertainty analysis is carried out on the measured data. The point is that assessing the short-ranged scale-effect is mandatory for characterising the transitional regime properly. Thus, the twofold approach mentioned before, consisting of a global and a local analysis, must be complemented with an uncertainty study accordingly.

The second shortcoming is that a bibliographic survey reveals a lack of works fulfilling the mentioned prerequisites altogether. Studies dealing with transitionally-operating airfoils abound [5, 12, 20–25], but either they consider the global or local approach alone [20, 21], they do not address the scale-effect as thoroughly as it should [5, 12, 24, 25] or, in case of doing so, they do not provide a proper uncertainty analysis for comparative purposes [22, 23]. Relevant differences occur in the aerodynamic behaviour even at Reynolds increments as low as 0.2×10^5 [23], which shows that a proper characterisation should consider such a short-ranged scale-effect. Addressing it requires a detailed protocolization of the measurement procedures for undertaking the global and local analyses, on the one hand, and a solid uncertainty study for establishing the relevance of the observed experimental differences, on the other hand. Fulfilling these two aims is the purpose of the work presented herein.

The paper is structured so that Section 2 presents the employed experimental set-up and describes the measurement protocols defined upon it, as well as detailing the surveying campaign. Section 3 includes the results and their corresponding discussions and, finally, Section 4 synthesises the main findings of the work and suggests possible future research lines.

2. Experimental set-up

This section consists of three parts: Section 2.1 details the physical scenario, Section 2.2 describes the measurement protocols and Section 2.3 presents the experimental schedule.

2.1. Physical scenario

Experimental aerodynamic studies are usually performed in wind tunnel set-ups, which are scientific-technological facilities that allow obtaining a constant airflow under controlled conditions. The set-up for the current research is an open-circuit wind tunnel with a rectangular cross-section of 0.75×1 m^2 and a 3-meters-long test-section. It is driven by a 37 kW fan capable of producing flows with peak velocities of 40 m/s in the test-section, and the maximum turbulence level within the operation range lies below 0.2% [30]. Further details on the specific layout of the tunnel and its characterization process may be found in [30, 31]. For illustrative purposes, a sketch of the set-up configured for undertaking measurements upon an airfoil is given in Figure 1.

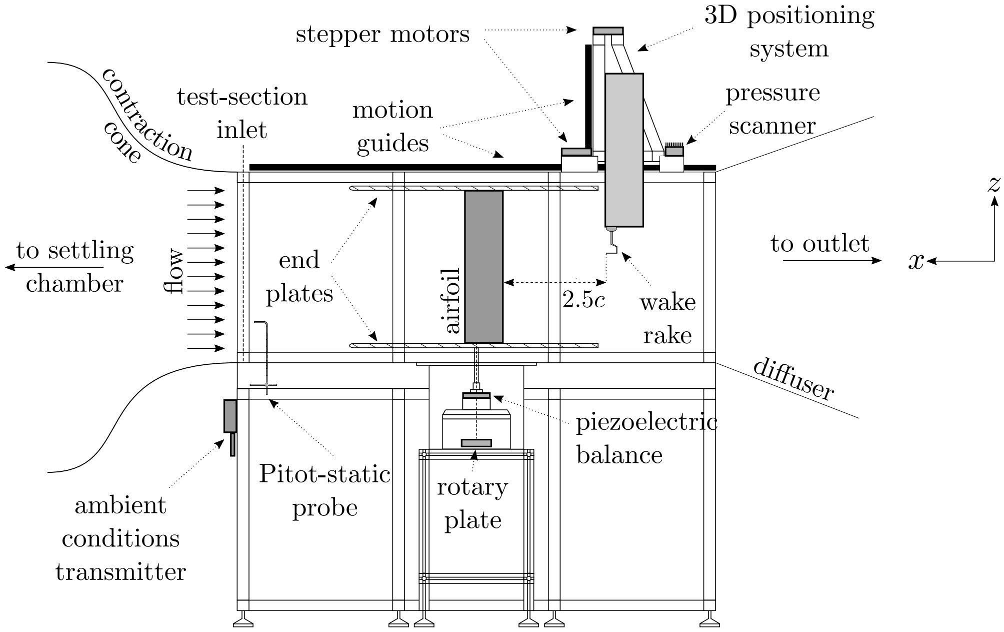

Figure 1: Schematic illustration of the wind tunnel set-up for undertaking measurements upon an airfoil.

The flow, coming from left to right, enters the test-section at a user-set velocity. A *Delta-Ohm HD2001.1* ambient conditions transmitter located there measures the temperature ($T_{\text{amb.}}$), relative humidity (RH) and atmospheric pressure ($p_{\text{amb.}}$), from which the upstream density (ρ_∞) and viscosity (μ_∞) are calculated following the humid-air model of Picard [32] and Zuckerwar [33], respectively. A *Delta-Ohm HD49047T01L* Pitot-static probe records the incoming flow's velocity (U_∞). The set ($U_\infty, \rho_\infty, \mu_\infty$) establish the Reynolds number together with the airfoil's chord. The velocity of the flow can be adjusted by modifying the fan's power, thus gaining control over the Reynolds number.
The airfoil is placed vertically above the central panel of the tunnel, and fixed by a metallic rod to a rotary plate standing in a sealed box underneath the tunnel's floor. Such a plate is driven by a remotely controlled *NI ISM 7400* stepper motor, thus achieving an angular degree of freedom around the z−axis of the tunnel that allows controlling the angle-of-attack. A *Kistler 9119AA2* piezoelectric balance is attached atop the plate, just beneath an auxiliary tool to which the metallic rod is fixed, thus measuring the loads and momenta that the flow exerts upon each of the axes of the airfoil. The two endplates delimiting the airfoil are located at a pre-established distance from its tips, so that three-dimensional effects are avoided and the two-dimensionality of the flow ensured. The airfoil-endplate distance corresponds to a ≈ 2 mm gap according to the estimations made by Torrano [30] following the work of Vaidyanathan et al. [34].
Between the airfoil and the diffuser, just after the endplates, a holder is attached to a three-axes positioning system, and enters the tunnel from the ceiling. Such a holder has a drilled hole at its tip for fixing different probes or measurement devices. Those devices undertake measurements that are required to be performed in several locations throughout the wind tunnel, which is why the positioning system is driven by three independent stepper motors of the type employed for the rotary plate, allowing the probes to move along the streamwise, transversal and vertical directions.

Pressure-related measurements are carried out by a *Scanivalve MPS4264* scanner, a differential device capable of measuring from a set of 64 ports simultaneously at a maximum rate of 850 Hz. The scanner is placed at the top of the wind tunnel, so that the length of the employed pneumatic lines is reduced in order to avoid compromising the dynamic response of the device.
The tested airfoil consists of a NACA0021 model owning a chordwise dimension of $c = 150$ mm and a span of $s = 900$ mm. The model has a set of orifices in its centre-line for installing pressure taps, and owns a hollow upper part so that such taps are taken to the pressure scanner from the ceiling. This modular design, as shown in Figure 2, ensures that both the load measurements and the surface pressure surveys are performed upon the same airfoil, thus avoiding experimental uncertainties that would have arisen in case different airfoil models had been employed. Further details on the manufacturing of the model are provided in [35]. The NACA0021 model has been chosen because of its application-agnostic nature, which allows focusing on the combination of measurement techniques employed herein, and not in a particular transitional application.

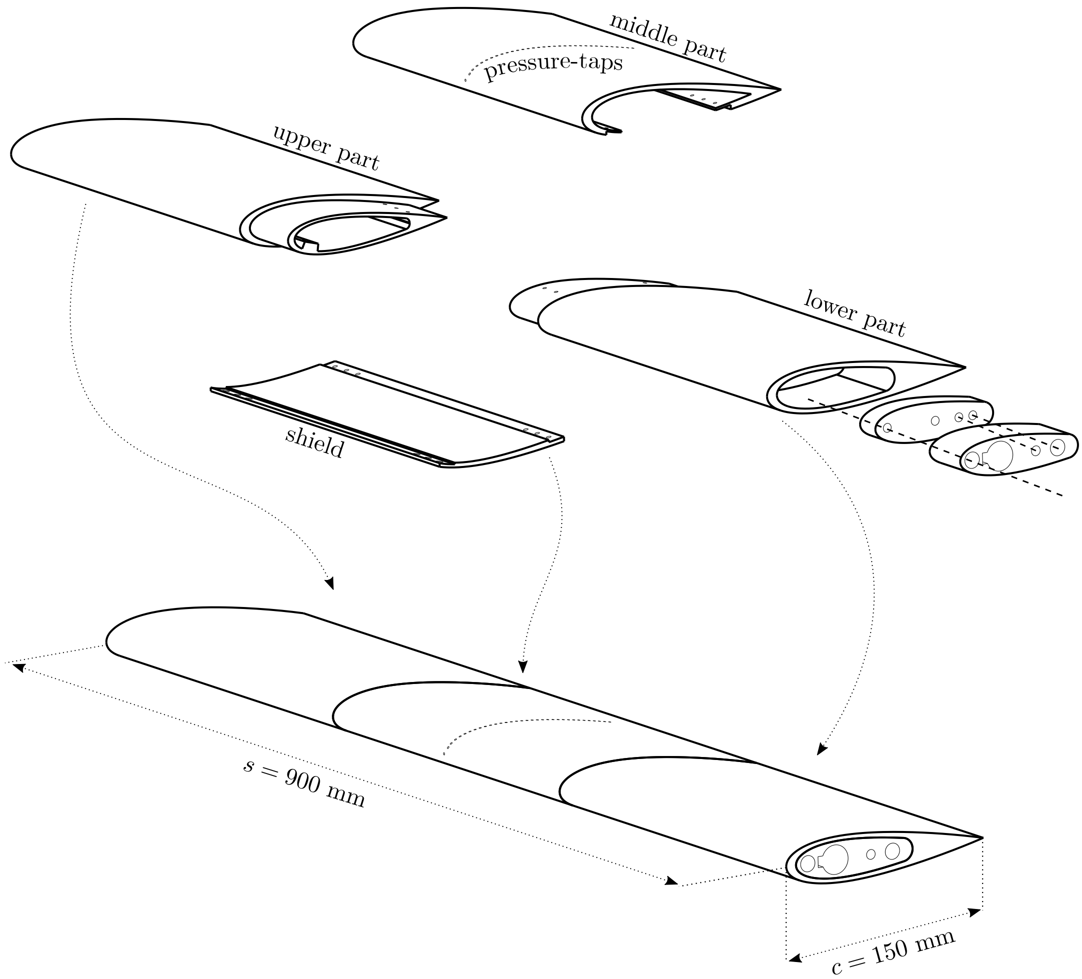

Figure 2: Schematic of the three-part modular assembly of the NACA0021 airfoil model.

2.2. Measurement protocols

These protocols establish standard ways for undertaking tests, thus ensuring the repeatibility of experiments. The basic measurement features of the probes shown in Figure 1 are gathered in Table 1.

According to Barlow et al. [36], it is necessary to establish a measurement period as large as for letting a fluid particle travel a distance equivalent to 10 test-section lengths if the statistical independence of the

Table 1: summary of measurement parameters.

Device	Period [sec]	Sampling rate [Hz]	Further considerations
Ambient conditions	5	8	–
Pitot-static probe		20	corrected for pressure and temperature effects [31]
Piezoelectric balance		500	corrected for electrical drift [31]
Pressure scanner		850	–

recorded signal is to be ensured. For a 3-meters-long test-section, achieving such a statistical convergence with a 5-seconds-long measurement period corresponds to an inlet velocity as low as 6 m/s, which is the minimum value that the wind tunnel system is able to provide without choking the fan. Such a 5-seconds period is maintained for every measurement prescribed in the protocols below.

The particular features of each device are its dynamic response or sampling rate, and any corrective measure it requires for whatever the technical reason. In case of the ambient conditions transmitter, the maximum rate is established at 8 Hz by the manufacturer, which is considered sufficient for recording the ambient variables acceptably. The Pitot-static probe has a sampling rate of 20 Hz, enough for monitoring the average velocity at the entrance of the test-section, as determining dynamic features of the incoming flow's profile is not necessary; the velocity is corrected for ambient pressure and temperature effects, according to the calibration chart provided by the manufacturer and as explained in a previous work of Zarketa-Astigarraga et al. [31]. The piezoelectric balance has a user-settable sampling rate ranging between $\left[10, 5\times10^3\right]$ Hz, which is set to 500 Hz following the method outlined by González et al. [37]; due to the small piezoelectric effect, an intermediate amplifier is necessary for recording the signal, which introduces an electrical drift that is corrected as detailed in a previous work by the authors [31]. The pressure scanner is employed for c_d and c_p measurements, which due to their dynamic nature require high sampling rates for being resolved adequately; such a rate is set to 850 Hz. The recordings of the measurement devices are carried out by *National Instruments* [38] data-acquisition modules assembled in a *cDAQ-9178* chassis connected to a CPU, which also controls the motion of the stepper motors and monitors the positions of the rotary plate and the three-axis system via a *cRIO-9031* controller. The overall system is monitored via a LabVIEW application [39] that is responsible for setting, activating and synchronising the collection of measurement devices and the set of stepper motors for driving both the rotary plate and the positioning system.

2.2.1. Alignment protocol

This protocol is for aligning the airfoil and the incoming flow, which is essential for establishing a reference angle-of-attack, namely a 0° configuration. As the NACA0021 airfoil is symmetric, the pressure of both sides will balance at such a configuration, yielding a null lift value. This feature does not depend on the Reynolds number of the flow and, consequently, the testing velocity at which the alignment protocol is carried out becomes irrelevant. The procedure consists of an angular route that parts from a negative angle-of-attack ($-\alpha_{\mathrm{max.}}$) and ends at its positive counterpart $\alpha_{\mathrm{max.}}$, varying the angle in steps of value $\Delta\alpha$ and performing load measurements with the piezoelectric balance. The values for $\alpha_{\mathrm{max.}}$ and $\Delta\alpha$ depend on the initial misalignment of the airfoil. If such a misalignment is small and the airfoil behaves linearly during the protocol, the resultant $c_l-\alpha$ curve corresponds to a straight line that crosses the $\alpha-$axis, showing where the 0° configuration lies. In case there exists a misalignment angle ($\alpha_{\mathrm{misal.}}$), a null c_l value does not correspond to the airfoil's current 0° configuration. If that occurs, it suffices with modifying the orientation of the airfoil by the quantity $\alpha_{\mathrm{misal.}}$, and repeating the protocol for corroborating that a proper alignment is obtained. The procedure is schematically outlined in Figure 3.

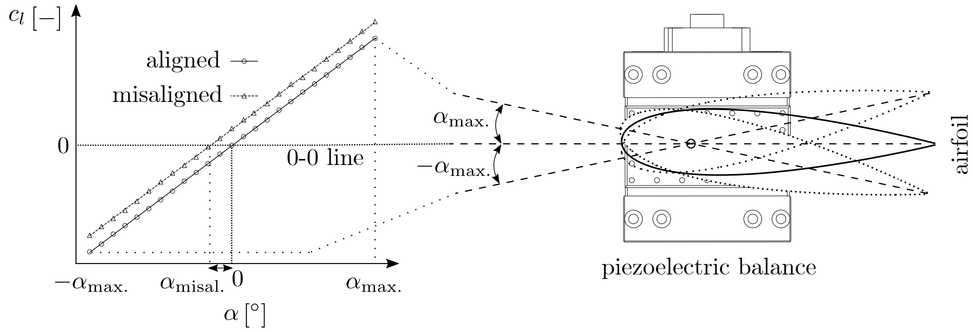

Figure 3: Schematic illustration of the alignment protocol.

2.2.2. $c_l - \alpha$ curve protocol

This protocol prescribes how a $c_l - \alpha$ curve is obtained for a given Reynolds number. The test is carried out by setting the tunnel operative and fixing a target Reynolds value. At each angular configuration, the flow is left to stabilize for a lapse of 2 seconds, after which the 5-seconds-long measurements are carried out, recording the values of $(p_{\text{amb.}}, T_{\text{amb.}}, RH, U_\infty)$ in addition to the loads. Such values are required for computing and maintaining a constant Reynolds number during the test, on the one hand, and to calculate the lift coefficient at the post-processing stage, on the other hand.
When the measurement task is over, the test proceeds with the next angular configuration. The airfoil is moved, the stabilization lapse awaited, and an additional measurement performed. The $c_l - \alpha$ curve is obtained when such steps are undertaken for each of the angles included in the route.
The post-processing stage includes two data-treatment operations. First, the measured forces are projected for obtaining the lift load, i.e. $l = f_{c\perp} \cos\alpha + f_{c\parallel} \sin\alpha$ (with $f_{c\parallel}$ and $f_{c\perp}$ being the measured loads, which are parallel and perpendicular, respectively, to the chordwise dimension, as depicted on Figure 4), and the lift coefficient is obtained by non-dimensionalising the load with $q_\infty \times c$, where $q_\infty = \rho_\infty U_\infty^2/2$ is the reference dynamic pressure. Second, a correction is applied to the coefficient so that it accounts for wall-interference effects, according to the formulæ provided by Selig et al. [40]. Indeed, the airfoil's blockage can grow as large as 8% for high angular configurations, for which the wall-interference corrections become mandatory.

2.2.3. $c_d - \alpha$ curve protocol

Drag measurements are carried out by the so called momentum-deficit method [11, 41, 42], which the authors have protocolized in a previous work for its application under conditions other than the clean flow paradigm [43]. Employing such a method has a well-founded rationale behind: in principle, three-axes piezoelectric balances can be used for measuring loads along three perpendicular directions. However, streamlined bodies such as airfoils show large lift-to-drag ratios under a widge range of flow configurations. Such a ratio, which is termed aerodynamic efficiency (E), can reach values of the order of ≈ 100 in devices like glider planes [44]. When using a multiaxial balance for measuring such disparate quantities, a cross-coupling may occur among its different axes [37]. Such a cross-coupling can affect the drag value significantly, given its relative smallness with respect to the lift force. The momentum-deficit method constitutes a trade-off solution that avoids turning drag measurements invalid from the standpoint of experimental acceptability. Such a method measures the velocity profile of the airfoil's wake. The interaction between the flow and the airfoil, whereby the flow loses part of its energy due to friction processes and pressure differences, causes a momentum deficit on the flow that gets manifested as a low velocity region downstream the airfoil. By combining mass and momentum conservation laws, it is possible to show that such a deficit corresponds to the drag force exerted upon the airfoil, which reads [11, 41]:

$$c_d = \int_{y'=0}^{y'=w'} \sqrt{\frac{p\left(y'\right)}{q_\infty}} \left(1 - \sqrt{\frac{p\left(y'\right)}{q_\infty}}\right) \mathrm{d}y' \ . \tag{1}$$

In Equation (1), $p\left(y'\right)$ is the total pressure profile measured along the transversal dimension of the tunnel at a downstream stage of the airfoil, which is why it depends on the dimensionless transversal coordinate $y' = y/c$. The integration takes place between $y' = 0$ and $y' = w'$, which represent transversal bounds on which the deficit of the wake becomes null and the flow regains its unperturbed condition.
On practical grounds, Equation (1) is evaluated by placing a wake-rake device at a certain distance downstream the airfoil and performing transversal surveys across the width of the tunnel. The downstream distance needs to be such the wake develops sufficiently for being measured by the wake-rake device with acceptable accuracy; according to Takahashi et al. [42], an extent of 2.5 chords shown in Figure 1 fulfills such a condition. The surveys must cover a distance long enough for traversing the wake entirely; empirically, it is found that the wake is widest for stalled configurations, with a length of $\ell_{\text{wake}} \approx 2{\times}c$ mm. However, the transversal dimension of the wake-rake device is of $\approx c/3$ mm, being necessary to perform a set of seven measurements for covering the total length of the wake. The transversal survey is divided into sections having the same length as the wake-rake; the central section is located behind the airfoil's trailing-edge when it is oriented in its 0° configuration, and the rest of the portions are placed a distance of $c/3$ away from each other, starting from the central section and filling the transversal dimension of the wind tunnel in both directions. Futher details about the $c_d - \alpha$ protocol may be found in [43].
As wall-interference corrections provided in [40] require performing lift and drag measurements together, a combined $c_l - c_d - \alpha$ protocol is designed. A schematic of such a protocol is outlined in Figure 4. For a given angular configuration, the wake-rake begins its transversal survey from $y' = 0$, which is located near the lower sidewall of the tunnel. The 2-seconds-lapse stabilization period is left before performing the measurement, after which the 5-seconds-long recording is executed. The probe is moved upwards, and the stabilization-recording cycle repeated, until the upper sidewall is reached. The lift measurement is performed when the wake-rake stands at the central section of the seven portions into which the transversal survey has been divided. Thus, each angular configuration consists of a single load measurement and seven wake-rake recordings that constitute a momentum-deficit curve.

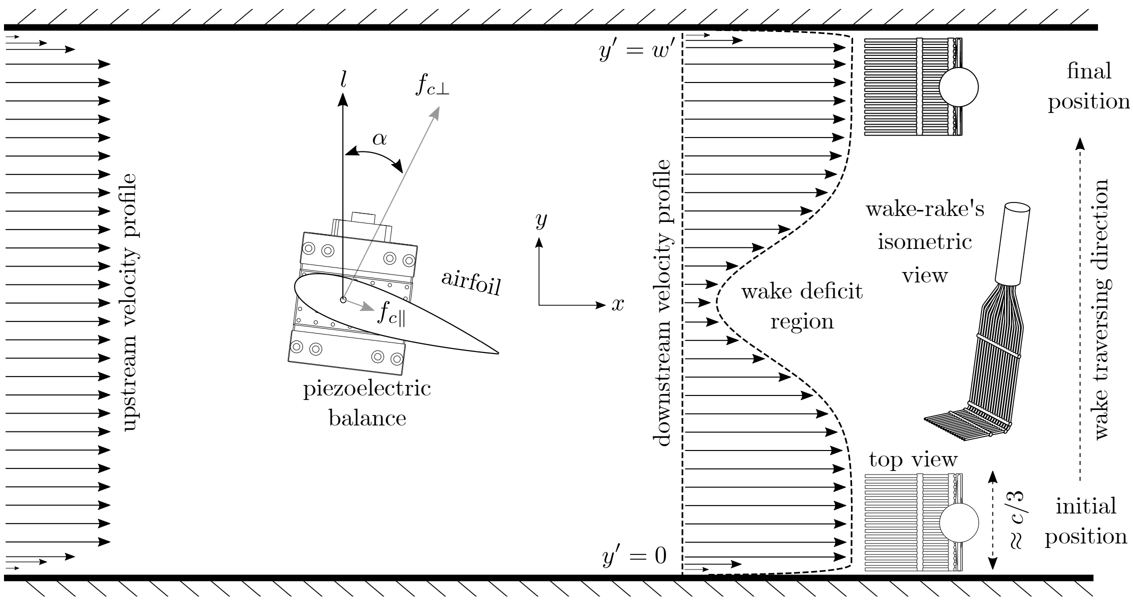

Figure 4: Schematic of the combined $c_l - c_d - \alpha$ protocol.

2.2.4. $c_p - x'$ curve protocol

This procedure is analogous to the $c_l - \alpha$ protocol. Instead of performing load measurements, a set of pneumatic lines are installed between the pressure-taps of the airfoil and the pressure scanner placed atop the tunnel. The tunnel is set at a given Reynolds number and angle-of-attack, and the flow left to stabilize for 2 seconds. Afterwards, a 5-seconds-long measurement is performed, which yields a $c_p - x'$ curve for such an angular configuration, with $x' = x/c$ being the dimensionless chordwise variable. The process is repeated for each of the angles comprising the route.

As the pressure-taps are located on a single surface of the airfoil, it turns necessary to mirror the angular route in order to obtain both the suction- and pressure-side distributions. Hence, the route consists of parting from a 0° configuration and increasing the angle until reaching $\alpha_{\text{max.}}$, after which it is decreased for closing the loop. This yields a set of $c_p - x'$ curves corresponding to the suction-side distributions of the airfoil. The same route is repeated for negative angles, thus obtaining the pressure-side curves.

The post-processing stage corrects the pressure measurements for a set of perturbing effects, such as the size and depth of the pressure-taps, the presence of burrs on their edges or the length of the pneumatic lines, according to Tropea et al. [45].

2.2.5. Visualization protocol

Flow visualization techniques refer to qualitative approaches that can assert the presence of certain fluid structures developed within a flowfield. LSBs, in particular, are well-suited for being identified by the so-called oil-film technique [50].

The oil-film technique consists of coating the airfoil surface with a thin layer of a coloured, oily material. The flow then sweeps the oil layer, which develops visible pattern on the surface. This pattern, if interpreted correctly, provides information on the structures developed along the airfoil.

The oil-film technique depends on the viscosity of the material by which the airfoil is coated, and choosing the proper mixture is usually a trial-and-error task. The current study employs a solution of sunflower oil seeded with titanium dioxide (TiO_2) powder. The sunflower oil comes has a low viscosity, which is necessary for enabling en effective sweeping of the layer in low-Reynolds (low velocity) configurations. The chromatic properties of the TiO_2 powder allow obtaining a neat contrast between the airfoil's surface and the oil patterns.

The visualization protocol begins by applying a thin layer of oil-powder mixture upon the airfoil surface, with the tunnel being inoperative. The layer is homogeneously spreaded throughout the surface, avoiding the formation of lumps that may affect the evolution of the flow. The airfoil is fixed at a given angular configuration, as the visualization technique is not dynamic, i.e. the patterns are meant to be representative of a given angular configuration and Reynolds number. Changing either of them while running the visualization turns the underlying traces invalid, as it is not possible to discern the effects of the different flow configurations upon the oil patterns. With the airfoil fixed, the tunnel is set at a given Reynolds number, and the oil traces let to develop. The lapse required for obtaining clear patterns may vary depending on the particular configuration of the flow. Once the traces are stabilised, visual evidences are gathered if the patterns show relevant features of the flow. The tunnel is stopped and the surface cleaned before proceeding with further visualizations.

2.2.6. Repeatibility protocol

This protocol prescribes that the measurement procedures described above must be repeated a minimum of three times for each tested configuration, so that an acceptable statistical convergence is obtained on the data. Such a convergence is quantified by undertaking a replication-level-based uncertainty analysis on the measured datasets, as explained in [51]. This analysis allows setting an uncertainty interval for each variable, and a generic parameter (ϕ) is expressed as:

$$\phi = \overline{\phi} \pm \delta_\phi \ \ (20 \text{ to } 1) \ , \tag{2}$$

where $\overline{\phi}$ is the average value of ϕ, δ_ϕ is its uncertainty interval and (20 to 1) means that the uncertainty analysis is carried out with a 95% confidence level, which is a standard practice in experimentalism [52–54].

A thorough uncertainty analysis of the wind tunnel system is carried out in the work of Zarketa-Astigarraga et al. [31]. Thus, the repeatability of the tests is ensured when the outcomes of successive measurements are shown to lie within the averaged uncertainty intervals of the measured variables, meaning that they converge to well-defined values.

2.3. Experimental schedule

In order to assess the short-ranged scale-effect mentioned in Section 1, the experimental campaign is designed following the work of Ananda [23]. The Reynolds numbers tested herein fall within the range $[0.8, 1.6] \times 10^5$, with increments of $\Delta\mathrm{Re} = 0.2 \times 10^5$ between adjacent configurations. Each of the Reynolds configurations is subjected to three different protocols: the $c_l - c_d - \alpha$ protocol, the $c_p - x'$ protocol and the visualization protocol.

The experimental effort required for undertaking such a campaign is estimated by considering that the $c_l - c_d - \alpha$ and $c_p - x'$ protocols are performed thrice for the sake of repeatability. For each Reynolds number, the resultant averaged curves amount to 3 in case of the $c_l - c_d - \alpha$ protocol (it yields the $c_l - \alpha$, $c_d - \alpha$ and $E - \alpha$ curves) and to 41 in the $c_p - x'$ one (a set of joint suction- and pressure-side distributions, one per angular configuration of the airfoil). The visualizations are not performed for each angle-of-attack, but merely for a subset of representative configurations ($\alpha \in [0, 12]^\circ$ with $\Delta\alpha = 3^\circ$) that can provide sufficient information about the evolution of the transitional structures. Knowing that the realisation of a $c_l - c_d - \alpha$ protocol takes an hour to complete and that the $c_p - x'$ and visualization protocols last 10 minutes approximately, it is possible to calculate the raw experimental time required for completing the campaign (disregarding other time-consuming actions such as experimental set-up and mounting, system error corrections or post-processing stages). Table 2 summarises the experimental effort of the current work.

Table 2: parametrical schedule for the experimental testing campaign.

	Tested Reynolds numbers	**Angular route**	**Averaged # of tests per Re**	**Total # of tests**	**Exp. time per Re [h]**	**Total exp. time [h]**
$c_l - c_d - \alpha$ **protocol**		$\alpha \in [0, 20]^\circ$, $\Delta\alpha = 1^\circ$ $\cup$ $\alpha \in [20, 0]^\circ$, $\Delta\alpha = -1^\circ$	3	15	3	15
$c_p - x'$ **protocol**	$\mathrm{Re} \in [0.8, 1.6] \times 10^5$, $\Delta\mathrm{Re} = 0.2 \times 10^5$		41	205	1/6	5/6
Visualization protocol		$\alpha \in [0, 12]^\circ$, $\Delta\alpha = 3^\circ$	5	25	5/6	25/6
			Sums			
			49	245	4	20

3. Results and discussion

The dataflow is organised following a top-bottom logic. The $c_l - \alpha$ and $c_d - \alpha$ curves, which represent angle-wise evolutions of the airfoil's global aerodynamic behaviour, are shown in Section 3.1. Surface pressure distributions and flow visualizations come in Section 3.2, which focuses on the local aspects of the flow. The correspondence beetween $c_p - x'$ distributions and c_l values is discussed next, highlighting the limitations of the local analysis.

3.1. *Analysis of global variables*

3.1.1. $c_l - \alpha$ *curves*

Figure 5 shows the $c_l - \alpha$ curves for different Reynolds numbers. The $x-$axis stands for the angle-of-attack, and the $y-$axis represents the lift coefficient. The angular route of the test has been outlined in Table 2. During such a route, the curves undergo a number of changes, describing a set of distinct regions. Those regions are delimited by the dotted vertical lines represented in the figure and, as observed, they depend on the Reynolds number, although the limits that correspond to the largest Re have been plotted for the sake of clarity. At low angular values, there exists a linear region where the curve follows a straight line, with the dashed line representing the potential-flow prediction and owning a nominal slope of atan (2π) [11]. Then there is a non-linear region, which is due to the effect of the LSB according to [24], where the evolution of the curve departs from the initial slope. At larger angles-of-attack the lifts saturate, and the curve bends downwards: that is the saturation zone. When the airfoil reaches a given angle, the lift value drops suddenly, showing what is known as the stall phenomenon. When stalling, the airofil stops behaving as a streamlined-body, and acts as a bluff-body instead. The zone beyond is termed the post-stall region, and the lift value does not vary significantly, remaining at relatively low values. This completes the forward angular route. However, things change when coming backwards, because pre-stall values are not regained at the same angular configuration at which stalling occurs. Instead, recovery happens at a lower-angle-of-attack. the difference between stalling and recovery creates a loop on the chart, which is known as aerodynamic hysteresis. Once pre-stall values are regained, the backward route finishes by returning to the initial position, completing the cycle.

The scale-effect is clearly addressed within the non-linear range. It is observed that at an angular configuration of six degrees the values show a vertical breakdown. The zoomed axes show that, when the uncertainty intervals are plotted for such a configuration, an overlapping happens just for the two lowest Reynolds cases, mainly because the uncertainty intervals are scale-effect-dependent as shown in a previous paper by the authors [31], and decrease progressively with an increase in Reynolds number. Anyhow, the analysis indicates that the chosen Reynolds increment is sufficient for inducing experimentally measurable changes. This does not occur when moving to the post-stall region, where the bluff-body behaviour of the airfoil breaks the scale-effect down and the curves collapse, showing overlapped uncertainty intervals that indicate undiscernible experimental data. These two facts highlight the relevance of owning, apart from a sufficiently sensitive piezoelectric balance, a well-established uncertainty analysis for identifying experimental differences within the short-ranged Reynolds increments employed in the tests.

3.1.2. $c_d - \alpha$ *curves*

Figure 6 represents the $c_d - \alpha$ evolutions for the set of Reynolds numbers described above. The diagram is similar to Figure 5, but the $y-$axis corresponds to the c_d in this case. However, there isn't an initial region of linear evolution as in the $c_l - \alpha$ cases, nor a subsequent non-linear zone. Instead, the curves show a low c_d region for small angles-of-attack, with the drag values not having clearly discernible evolutions and ranging between quasi-constant (Re = 1.6×10^5 case) and parabolic-like trends (Re = 0.8×10^5 case). The airfoil behaves as a streamlined body at those configurations, and the main contributor to c_d is the viscous drag, i.e. the viscous resistance coming from the boundary-layer itself. The curves are staggered vertically, with the lowest Reynolds number case showing the largest c_d value due to its relatively thicker boundary-layer, and *vice versa*. The zoomed axes plotted for the $\alpha = 3°$ configuration show that the Reynolds-dependent breakdown is as clear as in the lift curves, with the uncertainties comprising a set of non-overlapping intervals.

Stalling occurs after the low c_d region, with the drag values undergoing a sudden increase. Stalling and recovery trends are reproduced as in the $c_l - \alpha$ curves, with higher Reynolds number cases showing delayed stalls and earlier recoveries, as well as a larger hysteretic loop. The curves in the post-stall region collapse into the same homogeneous trends observed in Figure 5. The zoomed axes show a set of overlapping uncertainty intervals and indicate that the bluff-body behaviour within the post-stall region is not as Reynolds dependent as the pre-stall zone.

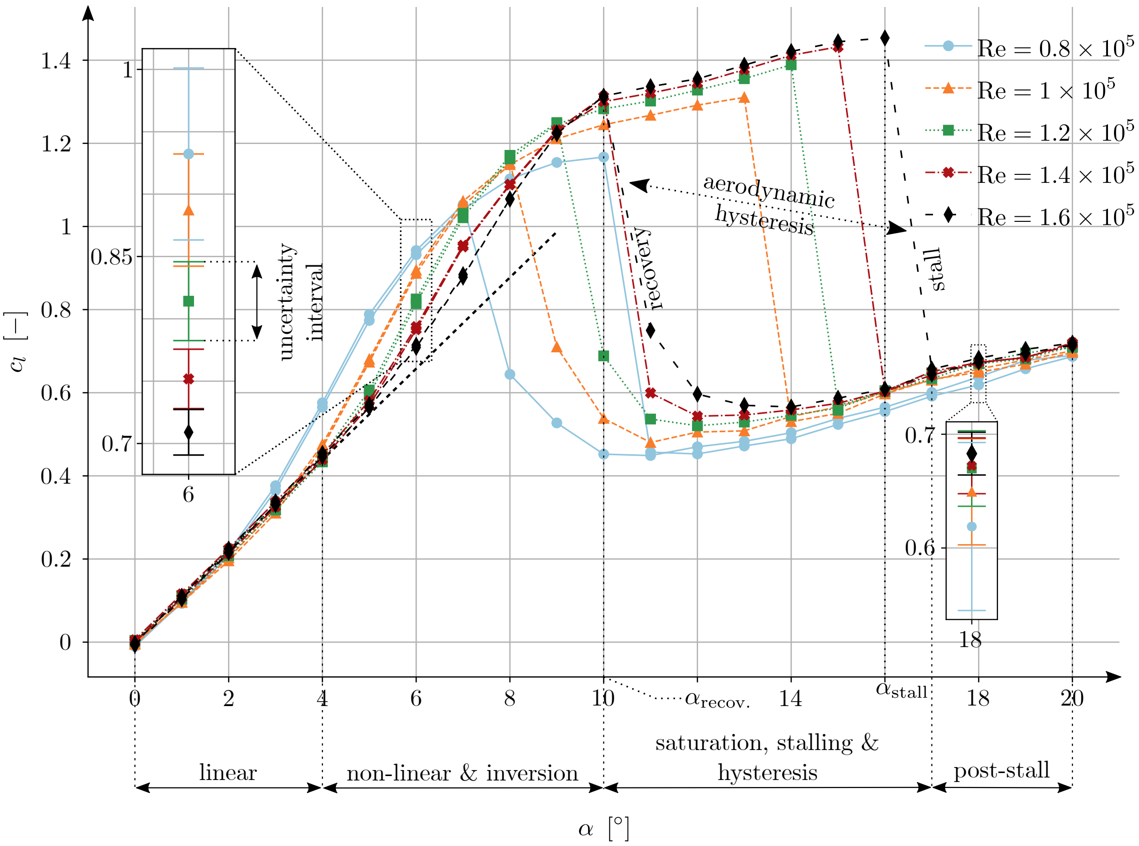

Figure 5: Reynolds effect on default $c_l - \alpha$ curves.

3.1.3. On the limitations of the global analysis

Figure 6 shows that the momentum-deficit technique is well-suited for capturing the drag differences of transitionally-operating airfoils in the short-ranged Reynolds number scope considered herein. However, one may wonder why such a technique should be employed when it is possible to measure the drag load directly by means of the piezoelectric balance. In fact, the experimental effort estimated in Table 2 is mainly dictated by the large amount of transversal surveys that the wake-rake has to perform for completing the protocol, a time-consuming task that can be reduced if the drag measurement technique is carried out by the piezoelectric balance.

The purpose of Figure 7 is to highlight the limitations of employing direct load measurements for calculating the drag force. The plot shows the $c_d - \alpha$ curves as obtained by the momentum-deficit method and the piezoelectric balance, for a Reynolds number of $1.2{\cdot}10^5$. The curves diverge noticeably, especially at low angles-of-attack; whereas the wake-rake technique provides a monotonously increasing drag value, the piezoelectric balance yields a parabolic curve within $\alpha \in [0, 14]^\circ$, reaching a minimum at $\alpha = 8^\circ$. Besides, the drag values become negative within the interval $\alpha \in [6, 10]^\circ$, which is clearly a cross-coupling effect coming from the contribution of the lift load; such a cross-coupling does not seem to have an effect at the post-stall region, where both techniques provide similar values, probably due to the bluff-body behaviour of the airfoil.

Anyhow, negative drag values make no physical sense, showing the ill-suitedness of the piezoelectric balance for measuring the drag force.

On the other hand, the uncertainty intervals of the load measurements are an order of magnitude higher than those of the wake-rake method, particularly at low angular configurations. This means that, if drag coefficients obtained by the piezoelectric balance were plotted for different Reynolds numbers, as in Fig-

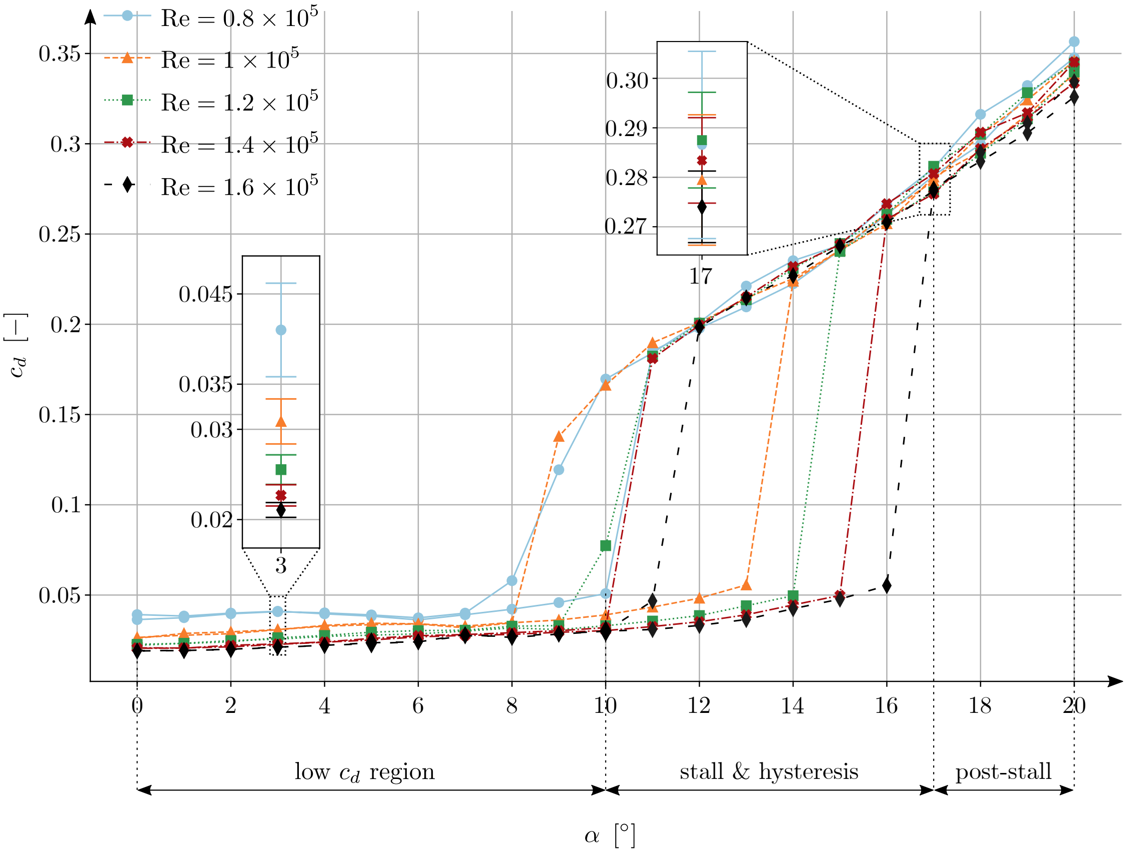

Figure 6: Reynolds effect on default $c_d - \alpha$ curves.

ure 6, the curves would not be discernible in terms of the experimental uncertainty. Hence, ascertaining the short-ranged scale-effect becomes unfeasible with the piezoelectric balance, which is an additional reason for considering it unsuitable for drag measurement purposes.

3.2. Analysis of local variables

The $c_l - \alpha$ and $c_d - \alpha$ curves provide a useful picture of the overall behaviour of an airfoil. However, it is instructive to consider how the flow develops along its surface locally, which can be helpful for designing control methods. The $c_p - x'$ distributions and the oil-painting visualizations cope with such local evolutions. The distributions provide the quantitative aspect, whereas the visualizations address the qualitative one.

3.2.1. Interpreting a visualization

Because of their inherently qualitative nature, visualizations need to be understood properly. Figure 8 provides a detailed interpretation of a visualization performed upon a generic flow configuration. The air flows from left to right, with the left hand-side of the figure corresponding to the leading-edge of the airfoil. There are three distinct regions that become clearly distinguishable on the flow patterns.
In a portion that extends downstream the leading edge, the flow sweeps the oil effectively and turns the underneath surface visible. That is the laminar region, where the flow remains attacked to the airfoil. The limit of such a region is marked by the separation line, beyond which oil traces begin to show up.
The region between the separation and reattachment lines corresponds to the LSB structure. The flow does not achieve an effective sweeping, as it is unable to reach the surface of the airfoil. During initial region, which stands between the separation and the recirculation line, the bubble is not as thick as to prevent the

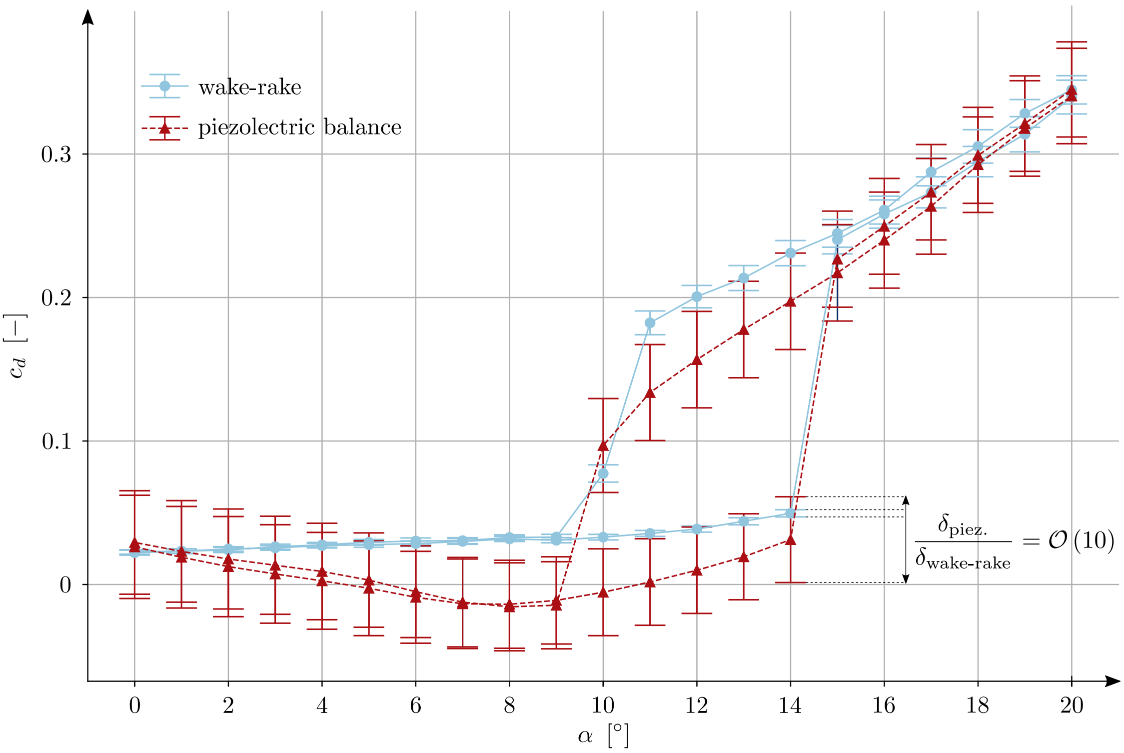

Figure 7: drag coefficients as calculated by different measurement techniques, namely the momentum-deficit method and the piezoelectric balance, for Re = $1.2{\cdot}10^5$.

sweeping completely, and the oil drops show a coalescing pattern. After the recirculation line, the height of the LSB avoids the flow to reach the surface, and the oil appears unswept. The recirculation line corresponds to the stage at which the reverse-flow vortex develops [27], causing the fluid to move in opposite directions at each of its sides and producing an accumulation of oil in the form of a thick drop that gets affected by the gravity force.

The turbulent region extends beyond the reattachment line. Initially, the oil gets effectively swept by the flow, but towards the trailing-edge the height of the boundary-layer grows exceedingly, and the flow begins to detach from the surface. Close to the edge, the air is unable to follow the surface of the airfoil, and a corresponding region of detached flow develops. The unswept zone represents such a zone.

3.2.2. Reynolds effects on $c_p - x'$ curves

The aerodynamic structures shown in Figure 8 change depending on the flow configuration. Figure 9 shows such changes when varying the Reynolds number of the flow. The set of pictures at the top correspond to the flow visualizations. The chart at the bottom represents the measured $c_p - x'$ distributions, with the x−axis standing for the dimensionless chordwise parameter and the y−axis being the c_p variable. The y−axis is inverted, with negative values standing on the upper side of the scale. The coefficients are relative to a static reference value taken at the entrance of the test-section, and the negative suction values are represented on an inverted y−axis complying with the convention in aerodynamic studies.

The curves correspond to the $\alpha = 6°$ configuration of the airfoil that, according to Figure 5, is the angle-of-attack at which the scale-effect becomes most noticeable. The shaded area on **??** represents the lift coefficient obtained by integration for the Re = $1.6{\times}10^5$ case [11]. Although pressure-side distributions show no appreciable differences, suction-side ones look as staggered as the c_l values, showing that the $c_p - c_l$ correlation holds. However, the progressive trend does not apply for the two largest Reynolds numbers, as the Re = 1.4×10^5 curve lies below the Re = 1.6×10^5 one along the chordwise dimension. So far, the authors have

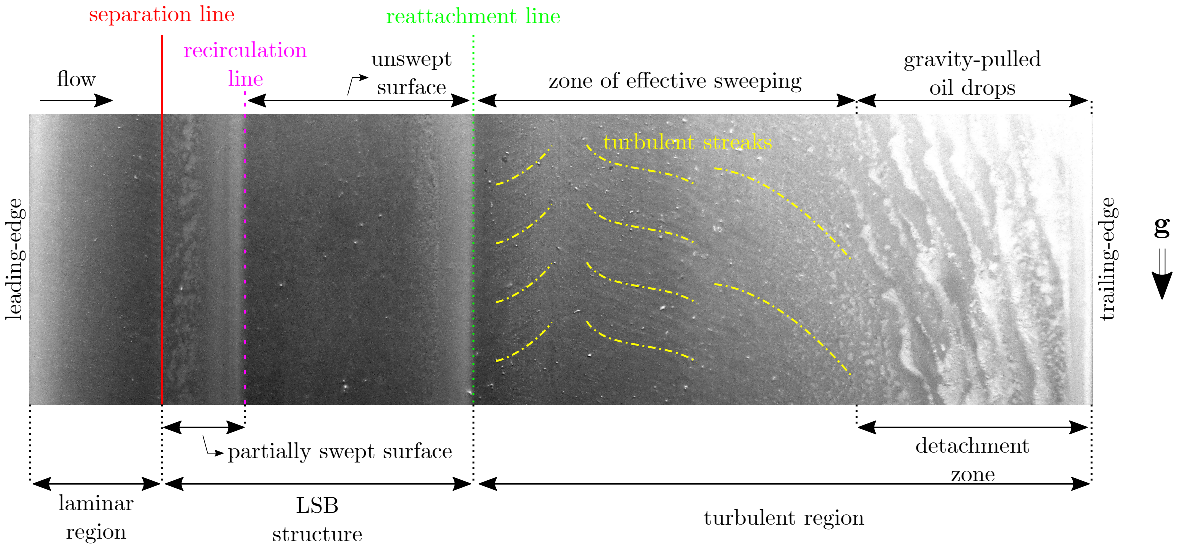

Figure 8: Interpretation of a generic visualization.

found no physical reason behind this behaviour. Nevertheless, the noticeably higher pressure-side recovery of the Re = 1.6×10^5 case turns the integration area smaller, and contributes less to the resultant lift value, agreeing with the trend observed in Figure 5.

The suction-side distributions show a strong suction peak near the leading-edge of the airfoil, followed by a pressure recovery that extends towards the trailing-edge. The region immediately downstream the suction peak shows a linear recovery trend. When compared against the visualizations, the separation lines are observed to fall within such a recovery region. The location of the separation phenomenon, marked by the red lines, moves sensibly downstream with increasing Reynolds numbers. The plateaus that follow the linear recovery region lie downstream the recirculation lines, where the air standing between the airfoil surface and the separated shear-layer is nearly still, making the pressure distribution constant. Reattachment correpsonds to the region of the distributions undergoing sharp gradients. The reattachment location, represented by the green lines, moves progressively upstream with increasing Reynolds numbers, and it is more dynamic than separation, depending sensibly on the value of the Reynolds number. Indeed, reattachment occurs when the flow has already undergone transition, whereas separation happens while the flow is still laminar. Given the fluctuating nature of turbulence, it makes sense to observe larger shifts in the positions of the reattachment line. With all, the bubble passes from covering the 30% of the chordwise extent at Re = $0.8{\times}10^5$ to representing the 20% of it at Re = $1.6{\times}10^5$, so the scale-effect on the shrinkage of the LSB is manifest. Post-reattachment recoveries are milder, mainly due to the turbulent fluctuations, which hinder a recovery as effective as in the laminar region.

Beyond $x' \approx 0.75$, the short physical distance between the suction- and pressure-sides of the airfoil does not allow introducing additional pressure-taps. Instead, the tendencies observed in the turbulent recovery region are extrapolated towards the trailing-edge. For the set of represented cases, the suction-side extrapolations fall below the pressure-side ones beyond a given chordwise stage. When compared against the visualizations, such stages are shown to agree with the detachment regions where the flow definitely separates from the surface. When the pressure-side extrapolations lie above the suction-side ones, the resultant pressure difference is negative and, consequently, its integration contributes negatively to the c_l value. That is why detached regions are said to be ineffective in producing lift.

3.2.3. α effects on $c_p - x'$ curves

Figure 10 shows the influence of the angle-of-attack on the local variables for Re = 1.2×10^5. Although the analysis is performed for a single Reynolds number for the sake of conciseness, the features discussed below are also found when comparing the rest of the Reynolds configurations angle-wise.

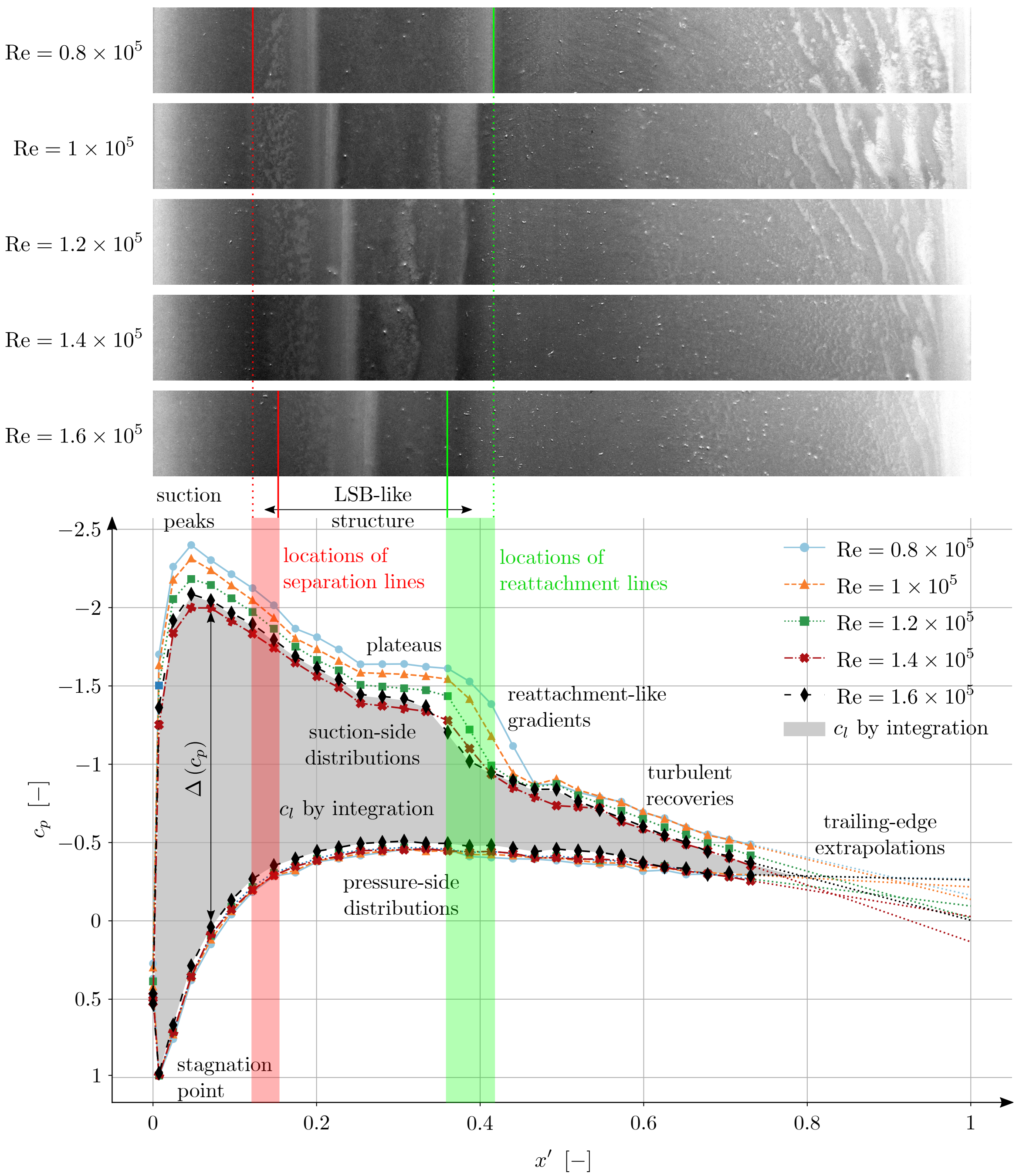

Figure 9: Reynolds effects on c_p curves and visualizations for $\alpha = 6°$.

When the angle-of-attack increases, the geometrical gradient near the leading-edge becomes steeper. The suction peaks become stronger and move towards the leading-edge, and the difference between suction- and pressure-side distributions also widens with α. For the 0° configuration, those distributions coincide due to the symmetry of the airfoil, which means that no lift is produced in accordance to Figure 5. Higher angles-of-attack increase the difference between pressure distributions and, consequently, the lift values obtained by integration are also larger, showing that the $c_p - c_l$ relationship holds.

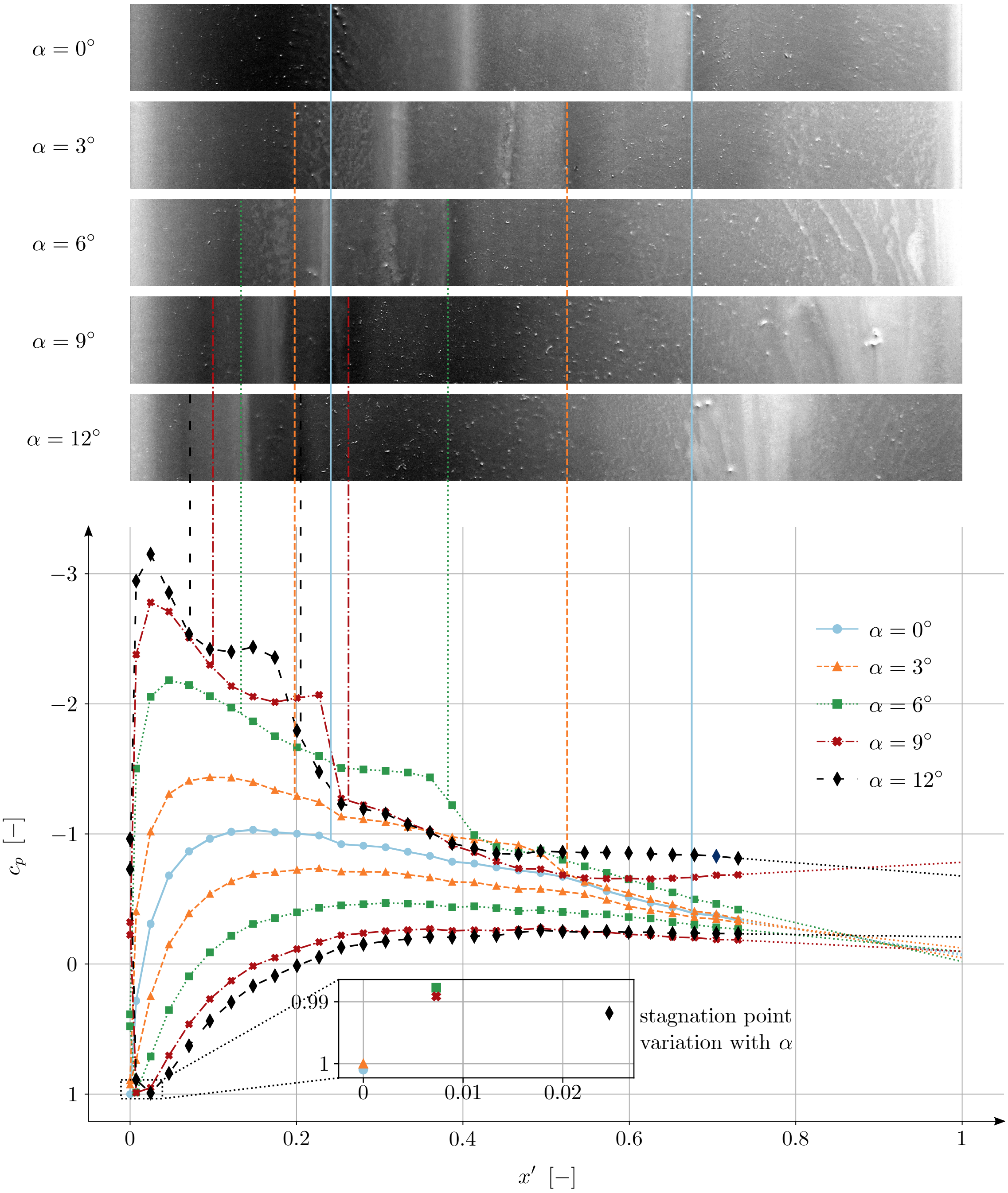

Figure 10: α effects on c_p curves and visualizations for Re = 1.2×10^5.

Regarding the evolution of the bubble, it is apparent that the LSB shrinks noticeably when increasing the angle-of-attack. Higher angular configurations induce an upstream motion of the separation line, and the bubble passes from covering a chordwise extent of ≈ 43% at $\alpha = 0°$ to representing the 13% of it at $\alpha = 9°$, which corresponds to a threefold reduction. Separation passes from being at a chordwise distance of 24% from the leading-edge to the 7% of it, and reattachment undergoes a noticeably larger upstream motion, going from the 70% to the 20%. This means that, for large α values, the laminar region and the LSB

get severely reduced, leaving the major part of the chord under turbulent conditions. The visualizations reveal such a fact, as the regions for which turbulent sweeping occurs become wider for higher angular configurations. In fact, it is observed that even the final detachment zone shifts upstream for the $\alpha = 12°$ case, leaving an unswept portion near the trailing-edge that is similar to the one developed inside the LSB.
An additional difference between Figures 9 and 10 comes from the locations of the stagnation points. On a stagnation point, the incoming flow decelerates until reaching a null velocity and, consequently, the measured quantity corresponds to the total pressure head. Usually, the stagnation point gets located near the leading-edge of the pressure-side, as it is the region where the flow impinges the airfoil directly. Reproducing stagnation points is relevant as it indicates that pressure measurements are being undertaken correctly and that the upstream dynamic head, namely q_∞, is a well-established reference value. In Figure 9, those points stand at the same chordwise position regardless the Reynolds number, which makes sense given the same angular configuration of the represented cases and the fact that stagnation is geometry-dependent. This dependency is made apparent in the zoomed axes at the bottom of Figure 10, which show that the points move slightly downstream with increasing angles-of-attack. On this respect, both the constancy observed in Figure 9 and the shift that occurs in Figure 10 indicate the validity of the measured c_p distributions.
A last distinction between Reynolds- and α-dependent effects has to do with the nature of the trailing-edge extrapolations at moderately high angles-of-attack. Until $\alpha = 6°$, both curves converge towards the trailing-edge of the airfoil and, eventually, the pressure-side distribution overcomes the suction-side one, indicating flow detachment. Instead, larger angles-of-attack show a sustained $\Delta(c_p)$, which results in larger c_l values when integrating the pressure differences. Quantitatively, this tendency for preserving a non-vanishing pressure difference agrees with the observed increase in lift values. Qualitatively though, the visualizations indicate that flow detachment is still present and, according to the interpretation given in Figure 9, such a detachment correlates with the collapse of the c_p distributions near the trailing-edge. The authors' interpretation for the different behaviours observed in Figure 10 is that, when the angle-of-attack gets large enough and the detachment zone begins to move upstream (which occurs, precisely, for $\alpha = 9°$), the collapse-based interpretation turns invalid.

3.2.4. On the limitations of the local analysis

Local variables provide relevant information about the effects that both the Reynolds number and the angle-of-attack induce on the aerodynamic structures. But the employed techniques also show certain limitations: regarding flow visualizations, their correlations with c_p curves have shown to break down at large angles-of-attack, especially near the trailing-edge of the airfoil. On this respect, the flow visualization technique stands as a qualitative tool that complements the aerodynamic analysis, but not as the core of the analysis itself.
Similarly, c_p distributions are essential for understanding the mechanisms of lift generation, as they provide the quantitative aspect of the visualizations. Furthermore, Meseguer & Sanz [11] express that c_l values can be obtained by c_p integration, linking the local and global approaches together. However, c_p distributions are measured at a particular cross-section of the airfoil, and considering that the integral of such distributions agrees with the global lift value requires two main assumptions: first, that the airfoil is homogeneous in its spanwise dimension. And, second, that the flow is two-dimensional inside the wind tunnel. On experimental grounds, those conditions are not fulfilled exactly, and the existing discrepancies induce differences on the $c_p - c_l$ correlations. Besides, pressure distributions and lift values are measured by different techniques, which can contribute to increasing the mismatches.
Figure 11 shows how such mismatches get manifested on the measured curves. Figure 11a represents two $c_l - \alpha$ curves obtained at $\mathrm{Re} = 1.2 \times 10^5$: the light blue curve corresponds to direct load measurements undertaken with the piezoelectric balance, while the dark red curve is derived from integrating the c_p distributions. Both techniques provide qualitatively similar trends: stalling and hysteresis are well captured by the c_p distributions, and the initial linear region matches quantitatively with the values obtained from the piezoelectric balance. However, the non-linear phenomenon is somewhat suppressed on the c_p-derived curve, and the post-stall behaviour is not as homogeneous. The set of uncertainty intervals attached to each data point explains these differences further, as the $c_l - \alpha$ curves may be classified into three distinct regions that behave differently from the standpoint of experimental uncertainty. On the leftmost region,

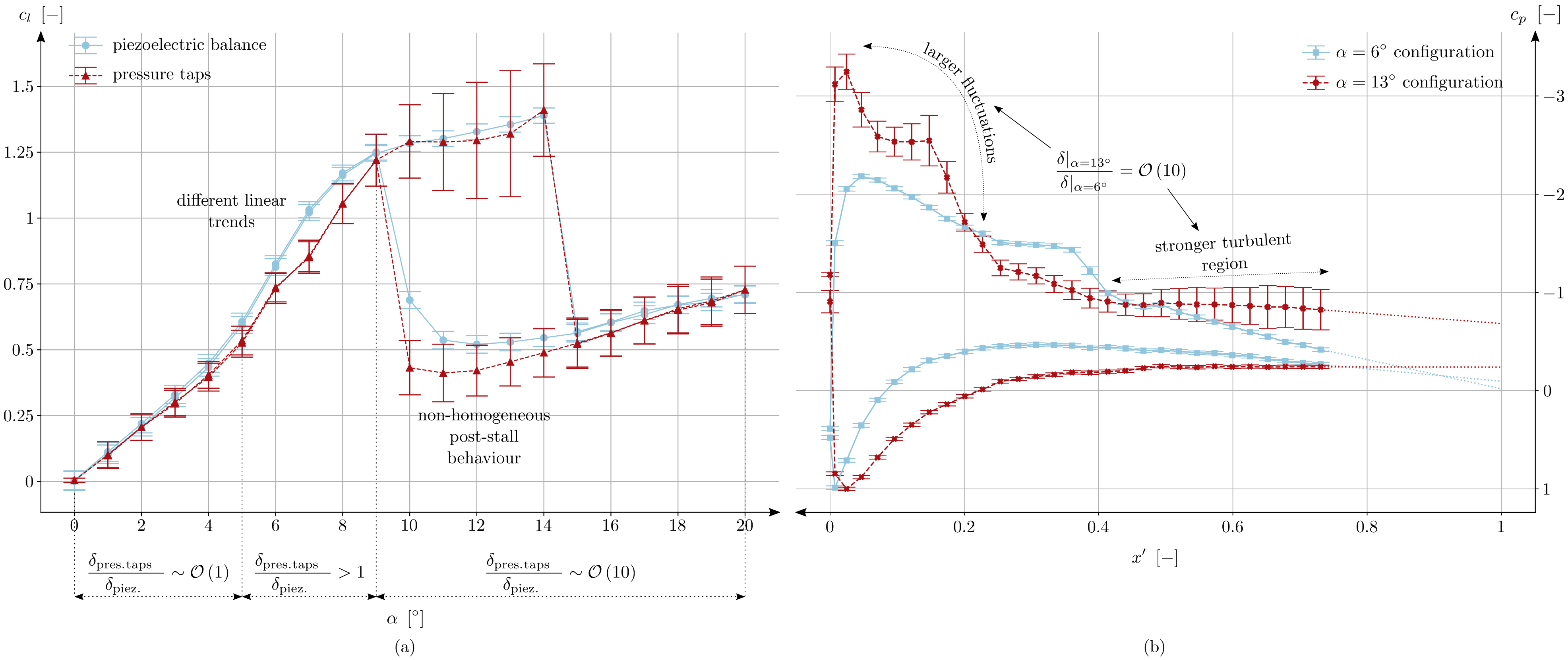

Figure 11: (a): $c_l - \alpha$ curves for Re = $1.2{\times}10^5$ obtained by different techniques; (b) c_p distributions corresponding to two different angles-of-attack.

both measurement techniques show uncertainty intervals of the same order of magnitude. For moderately higher angles-of-attack, lift values derived from c_p distributions own larger intervals than those coming from the piezoelectric balance. Within the hysteresis cycle and the post-stall region, the uncertainties of pressure measurements are an order of magnitude larger. On this respect, the piezoelectric balance shows a lower experimental uncertainty, and is better suited for obtaining c_l values via direct load measurements.

Figure 11b shows two c_p distributions measured at the same Reynolds number, but for different angular configurations, namely $\alpha = \{6, 13\}^\circ$. The uncertainty intervals attached to each data point vary appreciably when increasing the angle-of-attack. For the $\alpha = 6^\circ$ case, the amplitude of the uncertainties is homogeneous throughout the distributions, whereas the $\alpha = 13^\circ$ configuration shows substantial differences depending on the considered chordwise location and the chosen distribution. The uncertainty amplitudes of the pressure-side distribution are homogeneous, and similar in magnitude to their $\alpha = 6^\circ$ counterparts. But the suction-side intervals are an order of magnitude larger, and reflect a varying evolution along the chordwise dimension. The initial region is characterised by larger fluctuations, probably due to the dynamic nature of the separation line at $\alpha = 13^\circ$, which corresponds to a near-stall angular configuration. The intervals increase towards the trailing-edge of the airfoil, mainly because of the turbulent boundary-layer developed therein. In case of the $\alpha = 6^\circ$ configuration, reattachment occurs further downstream, and the turbulent layer does not have the necessary chordwise extent for developing effectively, which reduces the uncertainties of the measured data points.

With all, the uncertainty analysis highlights the limitations that a local magnitude has for representing a global variable. When a c_p distribution fluctuates noticeably, its correspondent lift value will reflect such a behaviour by showing a larger experimental uncertainty. Instead, the piezoelectric balance avoids the effect of such local fluctuations due to its inherently global approach. What Figure 11 remarks is the caution by which a local analysis needs to be applied, being aware of its limitations when correlating it with global variables. Hereon, c_p distributions and flow visualization are considered as qualitative tools that complement the analysis of global variables within the transitional regime.

4. Conclusions and future works

This work has focused on analysing the suitedness of a set of measurement techniques required for characterising the influence that both the Reynolds number and the angle-of-attack have on a transitionally-operating airfoil subjected to the clean-flow paradigm. On this respect, the most relevant findings can be classified in two main blocks: the ones related to the aerodynamic characterisation itself, which are enlightening from the standpoint of a design procedure. And the ones versing on the measurement techniques, which establish the range of applicability of the methods as well as their inherent limitations. Regarding the first of the blocks, the main conclusions are listed below:

- The uncertainty analysis has proven useful for addressing the scale-effect, showing that Reynolds number variations as small as $0.2{\times}10^5$ produce experimentally discernible changes on the global parameters. This indicates the high sensitivity of the aerodynamic structures with respect to the Reynolds number when operating at the transitional regime.
- The global analysis has yielded characteristic curves that agree qualitatively with those shown in the literature, either by Winslow et al. [12] or by Hansen et al. [24]. The departure from linearity of the $c_l - \alpha$ curves, the Reynolds-dependent inversion when reaching the saturation region, or the variations in stalling angles and hysteresis cycles have been thoroughly addressed and corroborated with previous results. However, the different testing conditions between the present work and [12], and the lack of an uncertainty analysis upon the datasets in [24], prevent the authors from taking the comparisons beyond the qualitative scope.
- The local analysis has asserted the formation of LSBs upon the airfoil, and show that they are sensibly affected by both the Reynolds number and the angular configuration. Increasing either of them causes a shrinkage of the bubble: in case of the scale-effect, the separation line moves downstream, whereas the reattachment one comes upstream, reducing the bubble by a 33% over the entire Reynolds range.

When increasing the angle of attack, both lines move towards the leading-edge, and the shrinkage can be as large as 75% when going from a 0° to a 12° configuration.

As for the second block, the following points synthesise the major findings:

- Although the piezoelectric balance is a well-suited device for obtaining lift loads, the cross-coupling effect among its axes turns it invalid for undertaking drag measurements. The comparison with the wake-rake method shows that the qualitative evolution of the curve does not conform with the expected behaviour, even providing negative drag values that lack any physical meaning. The large uncertainty intervals of the drag coefficients measured by the piezoelectric balance turn this technique unfeasible for addressing the short-ranged scale-effect considered herein.

- Pressure surface measurements provide relevant information on the local evolution of the airfoil, allowing to discern the separation and reattachment processes that determine the LSB structure. However, the integral correlation with lift values shows noticeable quantitative differences, even if the qualitative evolution of both curves is acceptable. On this respect, the validity of $c_p - x'$ curves is limited to the local scope, not being sensible to extrapolate a cross-sectional analysis to the entire airfoil. Similarly, flow visualizations allow ascertaining the presence of LSB structures on the airfoil, and they are shown to correlate acceptably with the pressure distributions. Nevertheless, their inherently qualitative nature should prevent experimenters from drawing any categorical conclusions based on their interpretation alone, complementing the analysis with a suitable quantitative technique instead.

- The set of different measurement techniques has proven successful in performing a combined characterisation approach at both the global and local scopes. Such an approach is relevant for acknowledging the effects of transitional structures thoroughly, as it provides a solid basis for studying further configurations and flow control techniques. Indeed, the flow conditions found in real world applications may differ greatly from those reproduced in experimental wind tunnels, and incorporating effects such as turbulence or surface roughness becomes a mandatory step in any design process concerned with characterising the behaviour of transitionally-operating airfoils. Likewise, the improvement of airfoils via flow control techniques such as vortex generators or similar passive methods requires owning a well-established characterisation protocol, so that the optimum distribution of those elements is correctly assessed. On this respect, the work undertaken herein may be considered a validation test of the set of measurement techniques employed.

5. Acknowledgements

The authors gratefully acknowledge the financial support from the Department of Education of the Basque Government for the Research Grant [PRE_2017_1_0178] and the Research Group [No. IT009-16].

References

[1] T. Mueller and J. DeLaurier. Aerodynamics of small vehicles. *Annual Review of Fluid Mechanics*, 35(1), 2003.

[2] Ralph J. Volino and Christopher G. Murawski. Separated flow transition in a low pressure turbine cascade - Mean flow and turbulence spectra. *American Society of Mechanical Engineers, International Gas Turbine Institute, Turbo Expo (Publication) IGTI*, 5 B(August):821–832, 2003.

[3] S. Watkins, S. Ravi, and B. Loxton. The effect of turbulence on the aerodynamics of low Reynolds number wings. *Engineering Letters*, 18(3), 2010.

[4] Luca Petricca, Per Ohlckers, and Christopher Grinde. Micro- and nano-air vehicles: State of the art. *International Journal of Aerospace Engineering*, 2011:1–17, 2011.

[5] Kenneth W. Van Treuren. Small-Scale Wind Turbine Testing in Wind Tunnels Under Low Reynolds Number Conditions. *Journal of Energy Resources Technology*, 137(5), 2015.

[6] Dhruvin L. Shukla, Amit U. Mehta, and Kalpesh V. Modi. Dynamic overset 2d cfd numerical simulation of a small vertical axis wind turbine. *International Journal of Ambient Energy*, 41(12):1415–1422, 2020.

[7] Jinjing Sun, Xiaojing Sun, and Diangui Huang. Aerodynamics of vertical-axis wind turbine with boundary layer suction – effects of suction momentum. *Energy*, 209:118446, 2020.

[8] Xu Zhang, Zhaoxuan Li, Xiang Yu, and Wei Li. Aerodynamic Performance of Trailing-Edge Modification of H-Type VAWT Blade Considering Camber Effect. *International Journal of Aeronautical and Space Sciences*, 21(3):587–598, 2020.

[9] Francesco Balduzzi, David Holst, Pier Francesco Melani, Felix Wegner, Christian Navid Nayeri, Giovanni Ferrara, Christian Oliver Paschereit, and Alessandro Bianchini. Combined numerical and experimental study on the use of gurney flaps for the performance enhancement of naca0021 airfoil in static and dynamic conditions. *Journal of Engineering for Gas Turbines and Power*, 143(2), 01 2021.

[10] Jinjing Sun and Diangui Huang. Numerical investigation of boundary layer suction control positions on airfoils for vertical-axis wind turbine. *Journal of Mechanical Science and Technology*, 35(7):2903–2914, 2021.

[11] José Meseguer-Ruiz and Ángel Sanz-Andrés. Procedimientos para determinar numéricamente la resistencia. In *Aerodinámica Básica*, chapter 9.2, pages 262–264. Garceta Grupo Editorial, 2 edition, 2012.

[12] Justin Winslow, Hikaru Otsuka, Bharath Govindarajan, and Inderjit Chopra. Basic understanding of airfoil characteristics at low Reynolds numbers (104–105). *Journal of Aircraft*, 55(3):1050–1061, 2018.

[13] Mark Thompson. *The Small Scales of Turbulence in Atmospheric Winds At Heights Relevant To MAVS*. PhD thesis, RMIT University, 2012.

[14] Jannik Schottler, Nico Reinke, Agnieszka Hölling, Jonathan Whale, Joachim Peinke, and Michael Hölling. On the impact of non-Gaussian wind statistics on wind turbines — an experimental approach. *Wind Energy Science Discussions*, (2007): 1–21, 2016.

[15] Anup KC, Jonathan Whale, and Tania Urmee. Urban wind conditions and small wind turbines in the built environment: A review. *Renewable Energy*, 131:268–283, 2019.

[16] G.P. Corten and H.F. Veldkamp. Insects Cause Double Stall. *European Wind Energy Conference 2001*, pages 470–474, 2001.

[17] Mohammed G. Khalfallah and Aboelyazied M. Koliub. Effect of dust on the performance of wind turbines. *Desalination*, 209:209–220, 2007.

[18] Mariana Kok, Tobias Mertens, Dominik Raps, and Trevor M. Young. Influence of surface characteristics on insect residue adhesion to aircraft leading edge surfaces. *Progress in Organic Coatings*, 76(11):1567–1575, 2013.

[19] Zhengru Ren, Amrit Shankar Verma, Ye Li, Julie J.E. Teuwen, and Zhiyu Jiang. Offshore wind turbine operations and maintenance: A state-of-the-art review. *Renewable and Sustainable Energy Reviews*, 144(January), 2021.

[20] Selig, Donovan, and Fraser. *Airfoils at Low Speeds*. Virginia Beach, VI, U.S.A, 1989.

[21] Michaels Selig, James J Guglielmo, Andy P Broeren, and Philippe Giguere. Summary of Low-Speed Airfoil Data. Technical report, University of Illinois at Urbana-Champaign, Virginia Beach, VI, U.S.A, 1995.

[22] M. Ol, B. McAuliffe, E. Hanff, U. Scholz, and C. Kähler. Comparison of Laminar Separation Bubble Measurements on a Low Reynolds Number Airfoil in Three Facilities. In American Institute for Aeronautics and Astronautics (AIAA), editor, 35^{th} *AIAA Fluid Dynamics Conference and Exhibit*, pages 1–11, Toronto, Ontario, Canada, 2005. American Institute for Aeronautics and Astronautics (AIAA).

[23] G. Ananda. *Aerodynamic performance of low-to-moderate aspect ratio wings at low Reynolds numbers*. PhD thesis, University of Illinois at Urbana-Champaign, 2012.

[24] K. L. Hansen, R. M. Kelso, A. Choudhry, and M. Arjomandi. Laminar Separation Bubble Effect on the Lift Curve Slope of an Airfoil. In 19^{th} *Australasian Fluid Mechanics Conference*, pages 1–4, Melbourne, 2014.

[25] Amanullah Choudhry, Maziar Arjomandi, and Richard Kelso. A study of long separation bubble on thick airfoils and its consequent effects. *International Journal of Heat and Fluid Flow*, 52, 2015.

[26] E. Reshotko. Transient Growth: a Factor in Bypass Transition. *Physics of Fluids*, 13(5):1067–1075, 2001.

[27] H. P. Horton. *Laminar separation bubbles in two and three dimensional incompressible flow*. PhD thesis, Queen Mary College, 1968.

[28] J. Watmuff. Evolution of a Wave Packet into Vortex Loops in a Laminar Separation Bubble. *Journal of Fluid Mechanics*, 397:119–169, 1999.

[29] M. Gaster. The Structure and Behaviour of Laminar Separation Bubbles. Technical report, Aeronautical Research Committee (ARC), London, UK, 1967.

[30] Ivan Torrano. *Low speed wind tunnel design, setup, validation and testing of airfoils in turbulent in ow conditions*. PhD thesis, Mondragon Goi Eskola Politeknikoa, 2016.

[31] Ander Zarketa-Astigarraga, Alain Martin-Mayor, and Manex Martinez-Agirre. Experimental uncertainty decompositions of aerodynamic coefficients affected by operative condition variations. *Measurement*, 165(C):1–14, 2020.

[32] A. Picard, R. S. Davis, M. Gläser, and K. Fujii. Revised formula for the density of moist air (CIPM-2007). *Metrologia*, 45(2):149–155, 2008.

[33] Allan J Zuckerwar and Roger W Meredith. Low-frequency absorption of sound in air. *Journal of Acoustical Society of America*, 78(September):946–955, 1985.

[34] Aditya Vaidyanathan, David Kingman, and Theresa Kurth. When do endplates work? In 52^{nd} *Aerospace Sciences Meeting*, pages 1–11, 2014.

[35] Ander Zarketa-Astigarraga. *Aerodynamic Characterization of Transitionally-Operating Airfoils under a set of Flow Conditions going from Ideal to Real Configurations.* PhD thesis, Mondragon Unibertsitatea, 2021.

[36] Jewel B. Barlow, William H Rae, and Alan Pope. *Low-speed wind tunnel testing.* John Wiley & Sons, Inc., 3 edition, 1999.

[37] M. A. González, J. M. Ezquerro, V. Lapuerta, A. Laverón, and J. Rodríguez. Components of a Wind Tunnel Balance: Design and Calibration. *Wind Tunnels and Experimental Fluid Dynamics Research*, pages 1–20, 2011.

[38] National instruments main page, . URL https://www.ni.com/en-us.html.

[39] Labview software main page, . URL https://www.ni.com/en-us/shop/labview.html.

[40] Michael Selig, Robert Deters, and Gregory Wiliamson. Wind Tunnel Testing Airfoils at Low Reynolds Numbers. In 49^{th} *AIAA Aerospace Sciences Meeting*, Orlando, FL, U.S.A, 2011.

[41] B. M. Jones. *The Measurement of Profile Dra by the Pitot-traverse Method.* Aeronautical Research Committee. Reports and memoranda. H. M. Stationery Office, 1936.

[42] On the decomposition of drag components from wake flow measurements. In 35^{th} *Aerospace Sciences Meeting and Exhibit*, number January, Reno, NV, U.S.A, 1997. American Institute for Aeronautics and Astronautics (AIAA).

[43] Ander Zarketa-Astigarraga, Alain Martin-Mayor, Manex Martinez-Agirre, and Markel Peñalba-Retes. Assessing the statistical validity of momentum-deficit-based c_D measurements in turbulent configurations. *Measurement*, 181, 2021.

[44] L.M.M. Boermans. Research on sailplane aerodynamics at Delft University of Technology. Recent and present developments . *Technical Soaring*, 30(1-2):1–25, 2006.

[45] Cameron Tropea, Alexander L. Yarin, and John F. Foss. Pressure Measurement Systems. In *Springer Handbook of Experimental Fluid Mechanics*, chapter 4, pages 179–214. Springer, Berlin, 1 edition, 2007.

[46] B. J. McKeon and A. J. Smits. Static pressure correction in high Reynolds number fully developed turbulent pipe flow. *Measurement Science and Technology*, 13(10):1608–1614, 2002.

[47] J.L. Livesey, J.D. Jackson, and C.J. Southern. The Static Hole Error Problem. *Aircraft Engineering*, pages 43–47, 1962.

[48] R. Shaw. The influence of hole dimensions on static pressure measurements. *Journal of Fluid Mechanics*, 7(4):550–564, 1960.

[49] C. Mayes, H. Schlichting, E. Krause, H.J. Oertel, and K. Gersten. *Boundary-Layer Theory.* Physic and astronomy. Springer Berlin Heidelberg, 2003.

[50] Wolfgang Merzkirch. *Flow Visualization.* Academic Press, 2 edition, 1987.

[51] Ander Zarketa-Astigarraga, Alain Martin-Mayor, and Manex Martinez-Agirre. Theoretical concepts for describing a replication-levels-based uncertainty analysis approach. In Sergey Yurish, editor, *Advances in Measurements and Instrumentation: Reviews, Book Series, Vol. 2.* IFSA Publishing, 1 edition, 2021.

[52] R. J. Moffat. The measurement chain and validation of experimental measurements. In *Acta Imeko, Proceedings of the* 6^{th} *Congress of the International Measurement Confederation*, volume 1, pages 45–53, Dresden, Germany, 1973.

[53] R. J. Moffat. Contributions to the Theory of Single-Sample Uncertainty Analysis. *Journal of Fluids Engineering*, 104: 250–258, 1982.

[54] R. B. Abernethy, R. P. Benedict, and R. B. Dowdell. ASME Measurement Uncertainty. *Journal of Fluids Engineering*, 107:161–164, 1985.

[55] Alexander Vorobiev, R M Rennie, and Eric J Jumper. Lift enhancement by plasma actuators at low reynolds numbers. *Journal of Aircraft*, 50(1):12–19, 2013.

[56] V. Alessandro, S. Montelpare, R. Ricci, and A. Zoppi. Numerical Modeling of the Flow over Wind Turbine Airfoils by Means of Spalart-Allmaras Local Correlation Based Transition Model. *Energy*, 130:402–419, 2017.

[57] B R McAuliffe and M Il Yaras. Separation-Bubble-Transition Measurements on a Low-Re Airfoil Using Particle Image Velocimetry. In *ASME Turbo Expo*, pages 1–10, Reno, NV, U.S.A, 2005. The American Society of Mechanical Engineers.